PHOTONICS Research

Controlling multiphoton excited energy transfer from Tm^{3+} to Yb^{3+} ions by a phase-shaped femtosecond laser field

Ye Zheng,[1],[†] Lianzhong Deng,[1],[†] Jianping Li,[1] Tianqing Jia,[1] Jianrong Qiu,[2] Zhenrong Sun,[1] and Shian Zhang[1],[3],*

[1]State Key Laboratory of Precision Spectroscopy, School of Physics and Materials Science, East China Normal University, Shanghai 200062, China
[2]State Key Laboratory of Silicon Materials, Zhejiang University, Hangzhou 310027, China
[3]Collaborative Innovation Center of Extreme Optics, Shanxi University, Taiyuan 030006, China
*Corresponding author: sazhang@phy.ecnu.edu.cn

The ability to control the energy transfer in rare-earth ion-doped luminescent materials is very important for various related application areas such as color display, bio-labeling, and new light sources. Here, a phase-shaped femtosecond laser field is first proposed to control the transfer of multiphoton excited energy from Tm^{3+} to Yb^{3+} ions in co-doped glass ceramics. Tm^{3+} ions are first sensitized by femtosecond laser-induced multiphoton absorption, and then a highly efficient energy transfer occurs between the highly excited state Tm^{3+} sensitizers and the ground-state Yb^{3+} activators. The laser peak intensity and polarization dependences of the laser-induced luminescence intensities are shown to serve as proof of the multiphoton excited energy transfer pathway. The efficiency of the multiphoton excited energy transfer can be efficiently enhanced or completely suppressed by optimizing the spectral phase of the femtosecond laser with a feedback control strategy based on a genetic algorithm. A $(1 + 2)$ resonance-mediated three-photon excitation model is presented to explain the experimental observations. This study provides a new way to induce and control the energy transfer in rare-earth ion-doped luminescent materials, and should have a positive contribution to the development of related applications.   © 2019 Chinese Laser Press

https://doi.org/10.1364/PRJ.7.000486

1. INTRODUCTION

The luminescence of rare-earth ions features excellent optical properties such as good optical stability, a long luminescence lifetime, large Stokes/anti-Stokes shifts, high conversion efficiency, and well-defined emission bands. As an effective luminescence process, the energy transfer in rare-earth ion-doped luminescent materials has attracted considerable attention. In the energy transfer process, a sensitizer ion absorbs one or multiple photons and is excited to a higher energy level; then the sensitizer ion transfers its energy to an activator ion, and finally the activator ion is pumped to a higher excited state. Here, two interacting ions can be of the same type or not. Usually, there are two kinds of energy transfer processes, i.e., radiative and nonradiative energy transfers. Radiative energy transfer requires an overlap between the emission spectrum of the sensitizer ion and the absorption spectrum of the activator ion, because a photon exchange between the two ions has to occur. However, a nonradiative energy transfer is accomplished via a Coulomb interaction under assistance of the host

phonons due to an energy mismatch [1]. Compared with radiative energy transfer, nonradiative energy transfer is more common in the luminescence process of rare-earth ions, and the energy transfer efficiency has a strong dependence on the distance between the two interacting ions.

Among all trivalent lanthanide ions, the Yb^{3+} ion has often been used as a good sensitizer for energy transfer, due to its simple energy level structure and a relatively large absorption cross section near infrared light. For example, Gouveia-Neto et al. demonstrated white light generation in Tm^{3+}/Ho^{3+}/Yb^{3+} co-doped glass using Yb^{3+} ions as the primary sensitizer for energy transfer [2]. Similar results were observed by Chen et al. in Tm^{3+}/Er^{3+}/Yb^{3+} co-doped glass ceramics [3]. In addition, energy transfer in various Yb^{3+}/Tm^{3+} co-doped samples has also been studied widely, and successive energy transfer processes from Yb^{3+} to Tm^{3+} ions have been recognized [4–6]. However, it is interesting that reverse energy transfer from Tm^{3+} to Yb^{3+} ions was observed experimentally, and two energy transfer pathways were assigned: one is a cooperative energy transfer

process of $Tm^{3+}(^1G_4) + 2Yb^{3+}(^2F_{7/2}) \rightarrow Tm^{3+}(^3H_6) + 2Yb^{3+}(^2F_{5/2})$ [7–11], whereas the other is the energy transfer process of $Tm^{3+}(^3H_4) + Yb^{3+}(^2F_{7/2}) \rightarrow Tm^{3+}(^3H_6) + Yb^{3+}(^2F_{5/2})$ [12,13].

In previous studies, energy transfer was usually observed under continuous laser excitation [7–13], and control of energy transfer efficiency was conventionally realized by varying dopant concentration [14], material structure [15–20], excitation laser power density [21], repetition rate [22], pulse duration [23], and so on. In this work, we first develop a phase-shaped femtosecond laser field to control the multiphoton energy transfer from Tm^{3+} to Yb^{3+} ions in co-doped glass ceramics. Compared with continuous laser excitation, femtosecond laser pulse excitation has the advantage of being able to induce the multiphoton absorption process due to high peak intensity, and so it can reveal some new up-conversion excitation pathways. In our experiment, Tm^{3+} ions are first pumped to a higher excited state via a multiphoton absorption process; then they transfer part of their energy to Yb^{3+} ions by decaying to a lower excited state or the ground state. Multiphoton energy transfer pathways are assigned by observing the laser power and polarization dependences of the luminescence intensities for Tm^{3+}/Yb^{3+} co-doped and Yb^{3+} single-doped glass ceramics. Importantly, the efficiency of multiphoton excited energy transfer can be greatly enhanced or completely suppressed by optimally controlling the spectral phase of the femtosecond laser field. Moreover, a $(1 + 2)$ resonance-mediated three-photon excitation model is employed to well explain the experimental observations.

2. EXPERIMENTAL ARRANGEMENT

Our experimental setup is shown schematically in Fig. 1. A Ti-sapphire mode-locked regenerative amplifier is used as the excitation source; it has a pulse duration of about 50 fs, a central wavelength of 800 nm, and a repetition rate of 1 kHz. The output femtosecond laser pulse is sent into a pulse shaper for shaping. The pulse shaper has a 4f configuration, which includes a pair of diffraction gratings of 1200 lines/mm each (G_1 and G_2), a pair of cylinder concave mirrors each of focal length 200 mm (C_1 and C_2), and a spatial light modulator (SLM). The SLM is programmable liquid crystal with
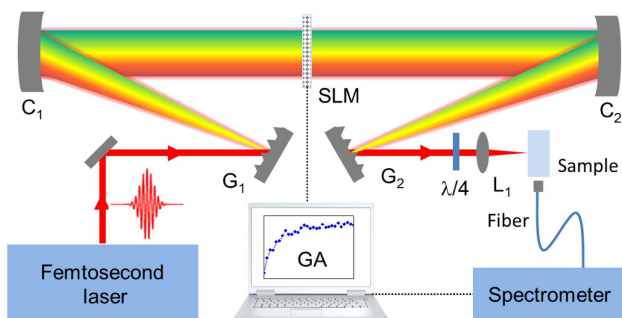
640 pixels, which is used to modulate the spectral phase in the frequency domain. The phase-shaped femtosecond laser pulse is focused into the sample by using a lens of 50 mm focus length. For laser polarization control, a quarter-wave plate is inserted in front of the focusing lens (L_1). The luminescence signal from the sample is detected at a vertical angle by a spectrometer via a collecting fiber.

The composition of the Tm^{3+}/Yb^{3+} co-doped glass ceramic sample for the experimental study is $50SiO_2–20Al_2O_3–30CaF_2–3TmF_3–1YbF_3$ (mol. %). We first mix high-purity raw materials and heat them to a temperature of 1450°C for about 1.5 h in a crucible at atmosphere pressure. Then we pour the melted mixture onto a brass mold and perform annealing at a temperature of 450°C for 10 h. Later, we increase the glass temperature 10°C per minute to 600°C and maintain the temperature for about 2 h. When the glass is finally cooled down to room temperature, the glass ceramic is obtained via crystallization. The sample is finely cut and polished before being used in the experiment. Yb^{3+} single-doped glass ceramics for comparison are also prepared in a similar way with the composition $50SiO_2–20Al_2O_3–30CaF_2–1YbF_3$ (mol. %).

The characterization of the Tm^{3+}/Yb^{3+} co-doped glass ceramic sample is shown in Fig. 2. A Bruker power diffractometer is used to perform X-ray diffraction (XRD) analysis, with its operating voltage and current being 40 kV and 40 mA, respectively. As shown in Fig. 2(a), six peaks can be clearly observed, indicating a cubic CaF_2 crystalline phase. Transmission electron microscopy (TEM) is also performed to further identify the nanocrystal structure. As shown in Fig. 2(b), the nanocrystals disperse uniformly in the glass. A high-resolution TEM image of individual CaF_2 nanocrystals is shown in Fig. 2(c). The lattice fringe can be clearly seen and its spacing is about 0.28 nm.

Figure 3(a) shows the absorption spectrum of the Tm^{3+}/Yb^{3+} co-doped glass ceramics in the UV–VIS–NIR spectral region. One can see four strong absorption bands around 355, 469, 684, and 789 nm, corresponding to the excited states of $^1D_2$, $^1G_4$, $^3F_{2,3}$, and $^3H_4$ of the Tm^{3+} ion,

Fig. 1. Schematic of the experimental setup. G_1 and G_2 are two diffraction gratings of 1200 lines/mm each. C_1 and C_2 are two cylindrical concave mirrors each of focus length 200 mm. SLM, spatial light modulator; $\lambda/4$, quarter-wave plate; L_1, focusing lens; GA, genetic algorithm.
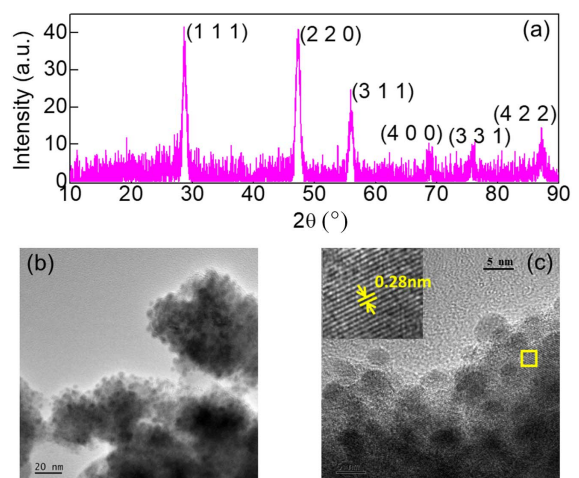

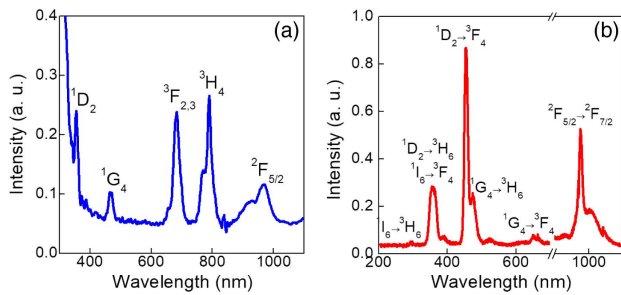**Fig. 2.** Characterization of the Tm^{3+}/Yb^{3+} co-doped glass ceramic sample. (a) XRD pattern. (b), (c) TEM images.

Fig. 3. (a) Absorption spectrum of the Tm^{3+}/Yb^{3+} co-doped glass ceramics in the UV–VIS–NIR region and (b) the luminescence spectrum of the same sample with the excitation of an 800 nm femtosecond laser pulse.

Fig. 4. Laser peak intensity dependences of (a) luminescence intensities at 355, 454, 473, and 975 nm for the Tm^{3+}/Yb^{3+} co-doped glass ceramics and (b) luminescence intensity at 975 nm for the Yb^{3+} single-doped glass ceramics, together with the absorption (lower right) and luminescence (upper left) spectra.

respectively. The very strong and broad absorption band appearing at an even shorter wavelength should be attributed to the highly excited states of the Tm^{3+} ion, such as $^1I_6$, $^3P_2$, $^3P_1$, and $^3P_0$. In addition, the absorption peak around 970 nm is ascribed to the excited state $^2F_{5/2}$ of the Yb^{3+} ion. Figure 3(b) shows the luminescence spectrum of the Tm^{3+}/Yb^{3+} co-doped glass ceramics under excitation of the 800 nm femtosecond laser field. The ultraviolet and blue emission bands are attributed to the state transitions of the Tm^{3+} ion: $^1I_6 \rightarrow ^3H_6$ (~290 nm), $^11I_6 \rightarrow ^3F_4$ (~346 nm), $^1D_2 \rightarrow ^3H_6$ (~362 nm), $^1D_2 \rightarrow ^3F_4$ (~454 nm), and $^1G_4 \rightarrow ^3H_6$ (~473 nm). The emission bands around 346 and 362 nm overlap partially in the spectrum with the center position at ~355 nm, and were difficult to be distinguished with our spectrometer. To facilitate later discussion, the two overlapping bands are denoted as the peak at 355 nm. The weak red emission band around 648 nm results from the state transition $^1G_4 \rightarrow ^3F_4$ of the Tm^{3+} ion. Moreover, the near-infrared emission band around 975 nm corresponds to the state transition $^2F_{5/2} \rightarrow ^2F_{7/2}$ of the Yb^{3+} ion.

3. RESULTS AND DISCUSSION

To explore the excitation mechanism of the observed luminescence in Fig. 2(b), we first study the dependence of luminescence intensity on the laser peak intensity. Usually luminescence intensity (I) and laser peak intensity (P) have the relationship $I \propto P^n$, where n is the number of photons [24]. Figure 4(a) shows the luminescence intensities at wavelengths of 355, 454, 473, and 975 nm as a function of laser peak intensity using a log-log plot, together with linear fitting. As can be seen, the slopes for the Tm^{3+} luminescence signals at 355, 454, and 473 nm are, respectively, 2.73, 2.76, and 2.71, which indicate that a three-photon absorption process should be involved. However, the slope for the Yb^{3+} luminescence signal at 975 nm is 2.05, indicating a more complex excitation mechanism. For comparison, we also study the dependence of luminescence intensity on laser peak intensity at 975 nm for the Yb^{3+} single-doped sample under the same laser excitation condition; the corresponding experimental result is shown in Fig. 4(b). The insets in the lower right and upper left are, respectively, the absorption and luminescence spectra of the Yb^{3+} single-doped glass ceramics. It can be seen that the fitting
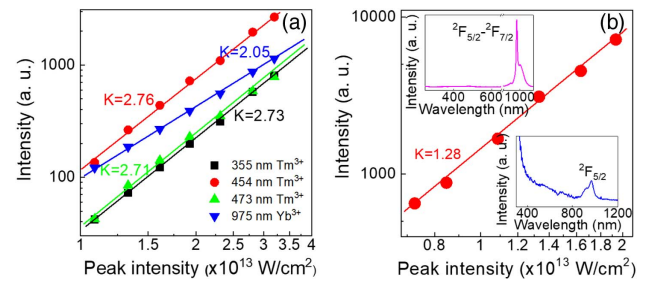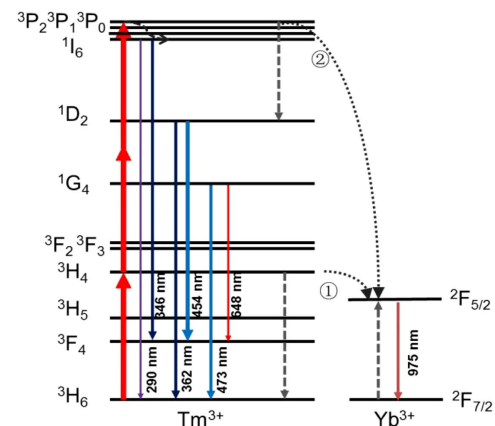

Fig. 5. Energy level structures of Tm^{3+} and Yb^{3+} ions, together with the proposed mechanisms for explaining the luminescence processes and the energy transfer from Tm^{3+} to Yb^{3+} ions.

slope is only 1.28. The increase of slope from 1.28 (Yb^{3+} ion) to 2.05 (Tm^{3+}/Yb^{3+} ions) indicates that an energy transfer from Tm^{3+} to Yb^{3+} ions should play an important role in the excitation process of the Yb^{3+} ion.

Based on the experimental observations above, we propose the following excitation mechanism to illustrate the luminescence processes and the energy transfer from Tm^{3+} to Yb^{3+} ions. As shown in Fig. 5, the population in the ground state $^3H_6$ of the Tm^{3+} ion is pumped to the intermediate state $^3H_4$ by a single-photon absorption, and then is further pumped to the excited states $^3P_{2,1}$ by a two-photon absorption, i.e., a $(1 + 2)$ resonance-mediated three-photon absorption process. The population in the excited states $^3P_{2,1}$ can nonradiatively or radiatively decay to the lower excited states $^1I_6$, $^1D_2$, and $^1G_4$, and emit these luminescence signals at the wavelengths of 290 nm ($^1I_6 \rightarrow ^3H_6$), 346 nm ($^1I_6 \rightarrow ^3F_4$), 362 nm ($^1D_2 \rightarrow ^3H_6$), 454 nm ($^1D_2 \rightarrow ^3F_4$), 473 nm ($^1G_4 \rightarrow ^3H_6$), and 648 nm ($^1G_4 \rightarrow ^3F_4$), as shown in Fig. 3(b). Considering the doping concentrations of the Tm^{3+} (3%)/Yb^{3+} (1%) ions and their energy levels, the energy transfer from Tm^{3+} to Yb^{3+} ions is most likely to occur via the following two pathways:

$Tm^{3+}(^3H_4) + Yb^{3+}(^2F_{7/2}) \rightarrow Tm^{3+}(^3H_6) + Yb^{3+}(^2F_{5/2})$ (①) and $Tm^{3+}(^3P_2) + Yb^{3+}(^2F_{7/2}) \rightarrow Tm^{3+}(^1D_2) + Yb^{3+}(^2F_{5/2})$ (②). Both the pathways are phonon-assisted energy transfer processes. Pathway ① involves a single-photon excitation and has been well explored in previous studies [12,13]. However, pathway ② includes a three-photon excitation and has never been observed in experiment, to the best of our knowledge. According to the Miyakawa–Dexter theory, the phonon-assisted energy transfer probability can be described as

$$W(\Delta E) = W(0) \exp(-\beta \Delta E), \quad \text{(1)}$$

where ΔE is the energy mismatch between the levels of the sensitizer and the activator; β is a parameter determined by the electron–lattice coupling and phonon nature of the material; and $W(0)$ is the probability with zero energy mismatch. The energy mismatch for pathway ② is only $\sim 100 \text{ cm}^{-1}$, which is much smaller than $\sim 2500 \text{ cm}^{-1}$ for pathway ① [25]. Obviously, the less the energy mismatch is, the larger the energy transfer probability will be. Moreover, the energy transfer efficiency is also proportional to the population of the sensitizer. Usually, the single-photon excited sensitizer in pathway ① has more population than that in pathway ②. Therefore, taking the two contributing factors into consideration, we believe that pathways ① and ② are two dominating pathways for the energy transfer from Tm^{3+} to Yb^{3+} ions; this will be further confirmed in the following study.

It is worth noting that a cooperative energy transfer (or quantum cutting) pathway, involving an excited-state Tm^{3+} sensitizer and a pair of ground-state Yb^{3+} activators, i.e., $Tm^{3+}(^1G_4) + 2Yb^{3+}(^2F_{7/2}) \rightarrow Tm^{3+}(^3H_6) + 2Yb^{3+}(^2F_{5/2})$, has been reported before [7–11]. However, the efficiency of the cooperative energy transfer was usually much lower than that of the normal energy transfer due to the double-operator nature [26]. Moreover, these cooperative energy transfer phenomena were usually observed in samples with relatively high doping concentrations of Yb^{3+} ions (>5%) and very large populations of Tm^{3+} sensitizers in the excited state $^1G_4$ [7–11]. For our case here, the doping concentration of the Yb^{3+} ion is just 1% and the population of the Tm^{3+} sensitizer in the excited state $^1G_4$ is rather small, as can be seen from the weak luminescence intensity at 473 nm ($^1G_4 \rightarrow ^3H_6$), as shown in Fig. 3(b). Therefore, the contribution of the cooperative energy transfer pathway to the excitation of the Yb^{3+} ion is ignorable in our experiment.

For further exploring the proposed energy transfer mechanism above, we study the laser polarization dependence of the luminescence intensities for both the Tm^{3+}/Yb^{3+} co-doped and Yb^{3+} single-doped samples. Typically, a quarter-wave ($\lambda/4$) plate is used to change the laser polarization. In theory, the multiphoton absorption in the broadband absorption system can be considered a sum of each individual transition. For convenience, we denote the states $^3H_6$, $^3H_4$, and $^3P_{2,1}$ as $|g\rangle$, $|i\rangle$, and $|f\rangle$, respectively. On the basis of the theoretical model of the atomic system with a narrow absorption line limit [27–29], the $(1+2)$ resonance-mediated three-photon transition probability in the final excited state $|f\rangle$ A_f can be approximated in the frequency domain as

$$A_f \propto \frac{1}{\hbar^6} \{[\cos^2(\theta) + \sin^2(\theta)] \times [\cos^4(\theta) + \sin^4(\theta)]\}$$
$$\times \int_{-\infty}^{\infty} G(\omega_f) \mu_{g \rightarrow i} \mu_{i \rightarrow f} |A_{\text{on-res}} + A_{\text{near-res}}|^2 d\omega_f, \quad \text{(2)}$$

with

$$A_{\text{on\_res}} \propto i\pi \int_{-\infty}^{+\infty} d\omega_i G(\omega_i) E(\omega_i) A^{(2)}(\omega_f - \omega_i), \quad \text{(3)}$$

$$A_{\text{near\_res}} \propto -\wp \int_{-\infty}^{+\infty} d\Delta \frac{1}{\Delta} E(\omega_i - \Delta) A^{(2)}(\omega_f - \omega_i + \Delta), \quad \text{(4)}$$

and

$$A^{(2)}(\Omega) = \int_{-\infty}^{+\infty} d\omega E(\omega) E(\Omega - \omega). \quad \text{(5)}$$

Here $\hbar$ is the Planck constant; $G(\omega_i)$ and $G(\omega_f)$ are, respectively, the absorption line-shape functions in the intermediate state $|i\rangle$ and the final state $|f\rangle$; $\mu_{g \rightarrow i}$ and $\mu_{i \rightarrow f}$ are, respectively, the effective dipole couplings for the state transitions of $|g\rangle \rightarrow |i\rangle$ and $|i\rangle \rightarrow |f\rangle$; and ω_i and ω_f are, respectively, the corresponding transition frequencies. The on-resonant term $A_{\text{on\_res}}$ in Eq. (3) represents the contribution of all on-resonant three-photon excitation pathways (i.e., $\Delta = 0$), whereas the near-resonant term $A_{\text{near\_res}}$ in Eq. (4) contains the contribution of other non-resonant three-photon excitation pathways (i.e., $\Delta \neq 0$), with $\wp$ being the Cauchy principal value. $E(\omega)$ is the Fourier transform of the electric field $E(t)$, and $E(\omega) = E_0(\omega) \times \exp[i\Phi(\omega)]$, with $E_0(\omega)$ and $\Phi(\omega)$ being the spectral amplitude and phase, respectively. θ is the angle between the input laser polarization direction and the optical axis of the $\lambda/4$ wave plate. The first term in the curly bracket, $[\cos^2(\theta) + \sin^2(\theta)]$, indicates the polarization dependence of the single-photon absorption for the state transition of $|g\rangle \rightarrow |i\rangle$. Since the value of this term is always unity for any angles of θ, it means the laser polarization does not affect the single-photon absorption. The second term, $[\cos^4(\theta) + \sin^4(\theta)]$, represents the polarization dependence of the nonresonant two-photon absorption for the state transition of $|i\rangle \rightarrow |f\rangle$. When $\theta = 2m\pi/4$ ($m = 0, 1, 2, \ldots$), the output laser is linearly polarized, and the value of this term is unity. When $\theta = (2m\pi + 1)/4$ ($m = 0, 1, 2, \ldots$), the output laser is circularly polarized, and the value is 1/2. For other values of θ, the output laser is elliptically polarized, and the value should fall within the range of [1/2, 1].

In our experiment, a $\lambda/4$ plate is inserted in front of the focusing lens (L_1) to vary the laser polarization, as shown in Fig. 1. The laser peak intensity after the $\lambda/4$ plate is measured to be about $1.21 \times 10^{13} \text{ W/cm}^2$. Figure 6(a) shows the luminescence intensities at 454 and 975 nm for the Tm^{3+}/Yb^{3+} co-doped glass ceramics upon varying the laser polarization (i.e., waveplate angle θ). Here, the solid lines are the theoretical calculation results. As can be seen, the normalized luminescence intensity at 454 nm decreases to 0.5 from 1.0 with the laser polarization changing from linear to circular. Obviously, this experimental observation is in good agreement with the theoretical prediction in Eq. (2). The laser polarization
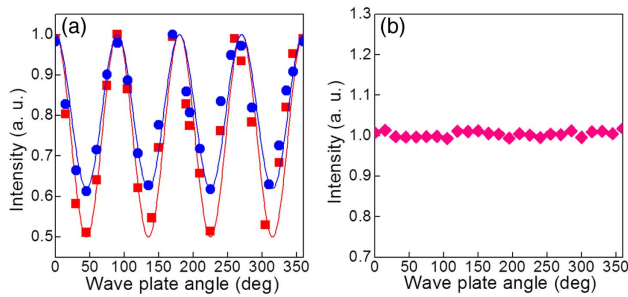
Fig. 6. Dependences of luminescence intensities on the value of θ, the angle between the direction of input laser polarization and the optical axis of the $\lambda/4$ plate. (a) Luminescence signals at 454 nm (red squares) and 975 nm (blue circles) for the Tm^{3+}/Yb^{3+} co-doped glass ceramics. (b) Luminescence signal at 975 nm (rose squares) for the Yb^{3+} single-doped glass ceramics.

dependences of the luminescence intensities at 355 and 473 nm can also be observed (not shown here), which indicates that the luminescence signals at 355, 454, and 473 nm should originate from the same excitation process of $(1 + 2)$ resonance-mediated three-photon absorption. However, when the laser polarization changes from linear to circular, the luminescence intensity at 975 nm decreases to 0.63 from 1.0. It is obvious that the control efficiency is smaller than that at 454 nm. For comparison, the laser polarization dependence of luminescence intensity at 975 nm for the Yb^{3+} single-doped sample is also measured and is shown in Fig. 6(b). One can see that the luminescence intensity, which is independent of the laser polarization, almost remains unchanged. The comparative study clearly shows that the energy transfer does happen from the Tm^{3+} to Yb^{3+} ions. There are two sources that contribute to the luminescence signal at 975 nm. One is the direct femtosecond laser excitation of the Yb^{3+} ion, which is not affected by

the laser polarization. The other is the energy transfer from the Tm^{3+} to Yb^{3+} ions, which is dependent on the laser polarization. The relative weight of the two sources determines the polarization control efficiency of the luminescence intensity at 975 nm. The experimental results in Fig. 6(a) indicate that the energy transfer from Tm^{3+} to Yb^{3+} ions is the major source of the luminescence signal at 975 nm.

As shown in Fig. 5 and Eq. (2), the energy transfer efficiency depends on the $(1 + 2)$ resonance-mediated three-photon transition probability. If the three-photon transition probability can be artificially manipulated, the energy transfer efficiency can be controlled efficiently. Typically, a spectral phase modulation can provide an effective tool to control the three-photon transition probability via constructive or destructive interference of the different excitation pathways. Here, we optimize the spectral phase of the femtosecond laser pulse by an adaptive feedback control strategy based on a genetic algorithm. The adaptive pulse-shaping method has been widely used as a robust search and optimization technique for studying many physical and chemical processes [30–32]. In our experiment, the luminescence intensity is used as the feedback signal (i.e., fitness function) to optimize the SLM phase mask. Initially, 150 phase masks are generated randomly with a personal computer and used as the first generation. Here, each mask is tested and ranked according to the luminescence intensity. The 10 best masks are selected and used as parents to produce 150 new masks in the next generation via crossover and mutation. The above process is repeated until the fitness function approaches convergence or the iteration number reaches a predetermined value.

We first enhance the energy transfer efficiency by adaptively shaping the laser's spectral phase. Here, the luminescence intensity at 975 nm of the Yb^{3+} ion is used as a feedback signal and is normalized to that with the transform-limited (TL) laser pulse excitation. As shown in Fig. 7(a-1), the luminescence
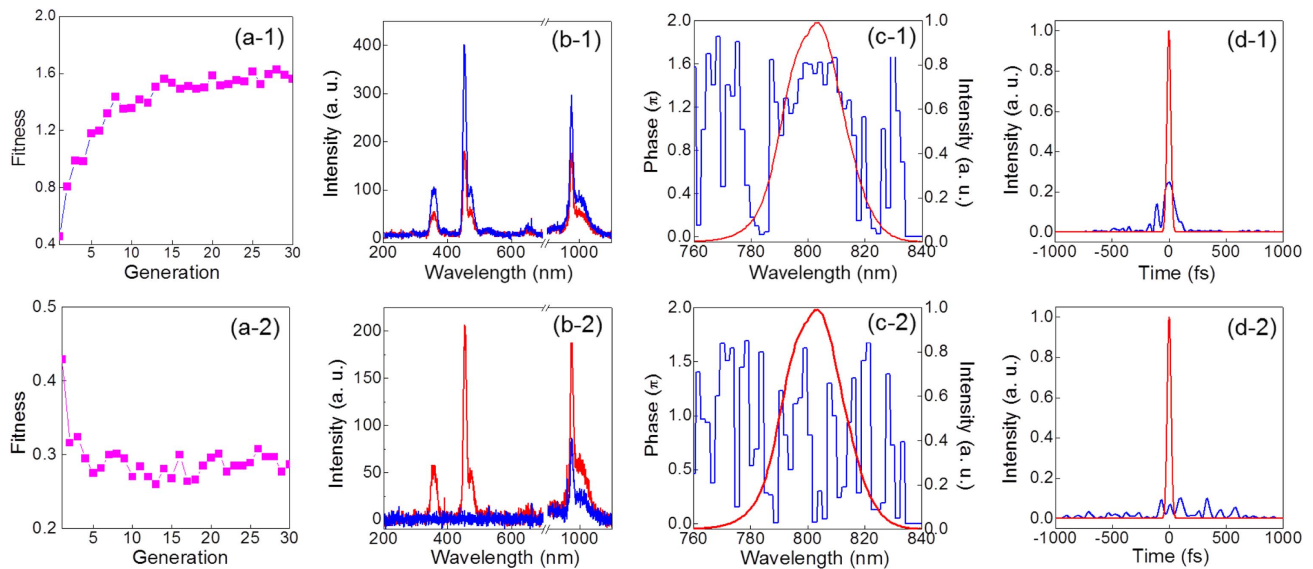

Fig. 7. Optimization processes for (a-1) enhancing and (a-2) suppressing the luminescence signal at 975 nm. Luminescence spectra of the Tm^{3+}/Yb^{3+} sample with (blue curve) and without (red curve) phase optimization for (b-1) optimal enhancement and (b-2) suppression. Phase masks (blue curve) and laser spectra (red curve) for (c-1) optimal enhancement and (c-2) suppression. Time profiles of the shaped (blue curve) and TL (red curve) femtosecond pulses for (d-1) optimal enhancement and (d-2) suppression.

intensity converges after optimization with 30 generations, which is enhanced by a factor of ∼1.6. For direct observation, the luminescence spectra with and without phase optimization are presented in Fig. 7(b-1). As expected, the luminescence signal at 975 nm is greatly enhanced. In addition, compared with the improvement factor of ∼1.6 at 975 nm for the Yb^{3+} ion, the luminescence intensity at 454 nm of the Tm^{3+} ion is increased by a factor of ∼2.3. This difference in the improvement factor can be explained as follows: as discussed above, in addition to multiphoton excited energy transfer, there are also other excitation processes for the Yb^{3+} ion that are not affected by spectral phase modulation. The optimized phase distribution is shown in Fig. 7(c-1), together with the laser spectrum (red curve). As one can see, the obtained optimal phase mask looks like a rectangle in the profile. A similar phase window has been used to increase the resonant two-photon absorption in a Rb atom [33]. We also numerically calculate the $(1 + 2)$ resonance-mediated three-photon transition probability based on Eqs. (2)–(5). The ratio of the transition probabilities with and without phase optimization is ∼2.5, which is very close to the improvement factor of ∼2.3 in our experiment. Based on the phase distribution in Fig. 7(c-1), the time profile of the shaped femtosecond pulse is as shown in Fig. 7(d-1), together with the TL laser pulse (red curve) for comparison. The shaped laser pulse is greatly broadened, and some side subpulses appear in front of the main pulse. It is worth pointing out that a similar improvement factor and optimal phase mask can also be obtained when the luminescence intensity at 454 nm of the Tm^{3+} ion is used as the feedback signal for optimization.

We then perform the same experiment to suppress the efficiency of energy transfer from Tm^{3+} to Yb^{3+} ions. Figure 7(a-2) shows the optimization process using the reciprocal of the luminescence intensity at 975 nm of the Yb^{3+} ion as the feedback signal. The normalized luminescence intensity is suppressed to ∼30% after 30 generations. Figure 7(b-2) shows the luminescence spectra with and without phase optimization. As can be seen, the luminescence signals of the Tm^{3+} ion disappear. This means that the energy transfer from Tm^{3+} to Yb^{3+} ions is completely suppressed. However, other excitation pathways are not affected by the spectral phase modulation, and they still contribute to the luminescence signal at 975 nm of the Yb^{3+} ion. The optimized phase distribution is examined and is shown in Fig. 7(c-2), and the laser spectrum is also shown (red curve). Obviously, the laser's spectral phase is modulated with a high frequency. Similarly, on the basis of the optimized phase distribution in Fig. 7(c-2), we also theoretically calculate the $(1 + 2)$ resonance-mediated three-photon transition probability. The transition probability can be suppressed to ∼0.1% after phase optimization, which is consistent with the experimental observation. Moreover, the time profile of the optimized femtosecond laser pulse is also given in Fig. 7(d-2), together with that of the TL laser pulse (red curve). One can see that the shaped laser pulse is now a series of subpulses. In addition, we also optimize this suppression using the reciprocal of the luminescence intensity at 454 nm of the Tm^{3+} ion as the feedback signal, and similar experimental results are obtained.

4. CONCLUSIONS

In summary, we have experimentally controlled the multiphoton excited energy transfer from Tm^{3+} to Yb^{3+} ions in codoped glass ceramics by using a phase-shaped femtosecond laser field with a feedback control strategy. Our experimental results showed that the Tm^{3+} ions are pumped to highly excited states via a multiphoton absorption, and then energy transfer occurs from excited-state Tm^{3+} sensitizers to ground-state Yb^{3+} activators. The energy transfer pathways were confirmed by observing the dependences of the luminescence intensities of the Tm^{3+}/Yb^{3+} and Yb^{3+} ions on the laser peak intensity and polarization. Our experimental results also showed that the efficiency of multiphoton energy transfer can be efficiently enhanced or completely suppressed by optimizing the spectral phase of the femtosecond laser, and the experimental observations can be well explained by considering a $(1 + 2)$ resonance-mediated three-photon excitation model. Our work demonstrates that spectral phase modulation of a femtosecond laser can provide a new alternative method to induce and control the energy transfer processes in rare-earth ion-doped luminescent materials, which should have important application prospects in related research areas such as white light generation or frequency conversion.

†These authors contributed equally to this work.

REFERENCES

1. T. Miyakawa and D. L. Dexter, "Phonon sidebands, multiphonon relaxation of excited states, and phonon-assisted energy transfer between ions in solids," Phys. Rev. B **1**, 2961–2969 (1970).
2. A. S. Gouveia-Neto, L. A. Bueno, R. F. Do Nascimento, E. A. da Silva, and E. B. da Costa, "White light generation by frequency upconversion in $Tm^{3+}/Ho^{3+}/Yb^{3+}$-codoped fluorolead germanate glass," Appl. Phys. Lett. **91**, 091114 (2007).
3. D. Chen, Y. Wang, K. Zheng, T. Guo, Y. Yu, and P. Huang, "Bright upconversion white light emission in transparent glass ceramic embedding $Tm^{3+}/Er^{3+}/Yb^{3+}$:β-YF_3 nanocrystals," Appl. Phys. Lett. **91**, 251903 (2007).
4. Q. Y. Zhang, T. Li, Z. H. Jiang, X. H. Ji, and S. Buddhudu, "980 nm laser-diode-excited intense blue upconversion in Tm^{3+}/Yb^{3+}-codoped gallate-bismuth–lead glasses," Appl. Phys. Lett. **87**, 171911 (2005).
5. G. Qin, W. Qin, C. Wu, S. Huang, D. Zhao, J. Zhang, and S. Lu, "Intense ultraviolet upconversion luminescence from Yb^{3+} and Tm^{3+} codoped amorphous fluoride particles synthesized by pulsed laser ablation," Opt. Commun. **242**, 215–219 (2004).
6. G. De, W. Qin, J. Zhang, J. Zhang, Y. Wang, C. Cao, and Y. Cui, "Infrared-to-ultraviolet up-conversion luminescence of YF_3:Yb^{3+}, Tm^{3+} microsheets," J. Lumin. **122**, 128–130 (2007).
7. S. Ye, B. Zhu, J. Luo, J. Chen, G. Lakshminarayana, and J. Qiu, "Enhanced cooperative quantum cutting in Tm^{3+}–Yb^{3+} codoped glass ceramics containing LaF_3 nanocrystals," Opt. Express **16**, 8989–8994 (2008).
8. Q. Y. Zhang, G. F. Yang, and Z. H. Jiang, "Cooperative downconversion in $GdAl_3(BO_3)_4$:RE^{3+}, Yb^{3+}(RE = Pr, Tb, and Tm)," Appl. Phys. Lett. **91**, 051903 (2007).
9. L. Xie, Y. Wang, and H. Zhang, "Near-infrared quantum cutting in YPO_4:Yb^{3+}, Tm^{3+} via cooperative energy transfer," Appl. Phys. Lett. **94**, 061905 (2009).

10. J. Li, J. Zhang, X. Zhang, Z. Hao, and Y. Luo, "Cooperative downconversion and near infrared luminescence of Tm^{3+}/Yb^{3+} codoped calcium scandate phosphor," J. Alloys Compd. **583**, 96–99 (2014).

11. X. Liu, Y. Qiao, G. Dong, S. Ye, B. Zhu, G. Lakshminarayana, D. Chen, and J. Qiu, "Cooperative downconversion in $Yb^{3+}–RE^{3+}$ (RE = Tm or Pr) codoped lanthanum borogermanate glasses," Opt. Lett. **33**, 2858–2860 (2008).

12. R. Wang, P. Zhang, S. Zhu, H. Yin, Z. Li, Z. Chen, Y. Zheng, G. Zhou, and J. Yu, "Spectroscopic analyses of $Tm^{3+}/Yb^{3+}:BaGd_2(MoO_4)_4$ crystal for mid-infrared applications," Infrared Phys. Technol. **94**, 1–6 (2018).

13. N. K. Giri, A. K. Singh, D. K. Rai, and S. B. Rai, "Role of Yb^{3+} and Tm^{3+} ions in upconversion emission of Tb^{3+} under 798 and 980 nm laser excitations in $Tb^{3+}–Tm^{3+}–Yb^{3+}$ doped tellurite glass," Opt. Commun. **281**, 3547–3552 (2008).

14. F. Wang and X. Liu, "Upconversion multicolor fine-tuning: visible to near-infrared emission from lanthanide-doped $NaYF_4$ nanoparticles," J. Am. Chem. Soc. **130**, 5642–5643 (2008).

15. X. Bai, H. Song, G. Pan, Y. Lei, T. Wang, X. Ren, S. Lu, B. Dong, Q. Dai, and L. Fan, "Size-dependent upconversion luminescence in Er^{3+}/Yb^{3+}-codoped nanocrystalline yttria: saturation and thermal effects," J. Phys. Chem. C **111**, 13611–13617 (2007).

16. Y. Sheng, L. D. Liao, A. Bandla, Y.-H. Liu, N. Thakor, and M. C. Tan, "Size and shell effects on the photoacoustic and luminescence properties of dual modal rare-earth-doped nanoparticles for infrared photoacoustic imaging," ACS Biomater. Sci. Eng. **2**, 809–817 (2016).

17. Y. Sun, Y. Chen, L. Tian, Y. Yu, X. Kong, J. Zhao, and H. Zhang, "Controlled synthesis and morphology dependent upconversion luminescence of $NaYF_4$:Yb, Er nanocrystals," Nanotechnology **18**, 275609 (2007).

18. J. Silver, M. I. Martinez-Rubio, T. G. Ireland, G. R. Fern, and R. Withnall, "The effect of particle morphology and crystallite size on the upconversion luminescence properties of erbium and ytterbium co-doped yttrium oxide phosphors," J. Phys. Chem. B **105**, 948–953 (2001).

19. Z. Bai, H. Lin, J. Johnson, S. C. R. Gui, K. Imakita, R. Montazami, M. Fujii, and N. Hashemi, "The single-band red upconversion luminescence from morphology and size controllable Er^{3+}/Yb^{3+} doped MnF_2 nanostructures," J. Mater. Chem. C **2**, 1736–1741 (2014).

20. G. S. Yi and G. M. Chow, "Water-soluble $NaYF_4$:Yb, Er (Tm)/$NaYF_4$/ polymer core/shell/shell nanoparticles with significant enhancement of upconversion fluorescence," Chem. Mater. **19**, 341–343 (2007).

21. X. Xue, M. Thitsa, T. Cheng, W. Gao, D. Deng, T. Suzuki, and Y. Ohishi, "Laser power density dependent energy transfer between Tm^{3+} and Tb^{3+}: tunable upconversion emissions in $NaYF_4$:Tm^{3+}, Tb^{3+}, Yb^{3+} microcrystals," Opt. Express **24**, 26307–26321 (2016).

22. C. F. Gainer, G. S. Joshua, and M. Romanowski, "Toward the use of two-color emission control in upconverting $NaYF_4$:Er^{3+}, Yb^{3+} nanoparticles for biomedical imaging," Proc. SPIE **8231**, 82310I (2012).

23. C. F. Gainer, G. S. Joshua, C. R. De Silva, and M. Romanowski, "Control of green and red upconversion in $NaYF_4$:Yb^{3+}, Er^{3+} nanoparticles by excitation modulation," J. Mater. Chem. **21**, 18530–18533 (2011).

24. M. Pollnau, D. R. Gamelin, S. R. Lüthi, H. U. Güdel, and M. P. Hehlen, "Power dependence of upconversion luminescence in lanthanide and transition-metal-ion systems," Phys. Rev. B **61**, 3337–3346 (2000).

25. R. M. El-Agmy, N. M. Al-Hosiny, S. Abdallah, and M. S. Abdel-Aal, "Generation of short wavelength in up-conversion of Tm^{3+} doped fluoride glass and its application in fiber lasers," J. Mod. Phys. **5**, 123–127 (2014).

26. F. Auzel, "Upconversion and anti-stokes processes with f and d ions in solids," Chem. Rev. **104**, 139–174 (2004).

27. D. Meshulach and Y. Silberberg, "Coherent quantum control of multiphoton transitions by shaped ultrashort optical pulses," Phys. Rev. A **60**, 1287–1292 (1999).

28. A. Gandman, L. Chuntonov, L. Rybak, and Z. Amitay, "Coherent phase control of resonance-mediated (2+1) three-photon absorption," Phys. Rev. A **75**, 031401 (2007).

29. S. Xu, Y. Huang, Y. Yao, T. Jia, S. Ding, S. Zhang, and Z. Sun, "Polarization control of intermediate state absorption in resonance-mediated multi-photon absorption process," J. Phys. B **48**, 135402 (2015).

30. M. Aeschlimann, M. Bauer, D. Bayer, T. Brixner, F. Javier García de Abajo, W. Pfeiffer, M. Rohmer, C. Spindler, and F. Steeb, "Adaptive subwavelength control of nano-optical fields," Nature **446**, 301–304 (2007).

31. J. L. Herek, W. Wohlleben, R. J. Cogdell, D. Zeidler, and M. Motzkus, "Quantum control of energy flow in light harvesting," Nature **417**, 533–535 (2002).

32. C. Brif, R. Chakrabarti, and H. Rabitz, "Control of quantum phenomena: past, present and future," New J. Phys. **12**, 075008 (2010).

33. N. Dudovich, B. Dayan, S. M. G. Faeder, and Y. Silberberg, "Transform-limited pulses are not optimal for resonant multiphoton transitions," Phys. Rev. Lett. **86**, 47–50 (2001).